RESEARCH ARTICLE

Bottom-Up Designed Porous Coaxial Twin-Electrodes for Efficient Redox Cycling

Tatjana Šafarik, Aleksandar Karajić, Stéphane Reculusa, Philip N. Bartlett, Nicolas Mano, and Alexander Kuhn*

Redox cycling (RC) is a powerful tool capable of amplifying faradaic currents in electroanalytical measurements, thus allowing an enhancement of sensitivity through fast multiple sequential oxidation and reduction reactions of a redox-active analyte. Present state-of-the-art RC devices are mostly based on planar electrode geometries either in 2D or 3D configurations, requiring cleanroom facilities and expensive microfabrication techniques. Here, the electrochemical elaboration and characterization of a 3D coaxial macro-porous twin-electrode is reported, obtained by following a low-cost bottom-up approach. A nanoengineered highly organized porous material is the basis for the design of two threaded cylindrical porous gold micro-electrodes with a gap in the micrometer range that can be fine-tuned. The potentials of the outer and inner electrodes are biased at values above and below the redox potential of the analyte so that a given molecule can participate several times in the electron exchange reaction by shuttling between both electrodes. The resulting signal amplification, combined with a straight-forward synthesis strategy of the electrode architecture, allows envisioning numerous (bio)electroanalytical applications.

T. Šafarik, S. Reculusa, A. Kuhn
Univ. Bordeaux
ISM
CNRS UMR 5255
Bordeaux INP
16 Avenue Pey Berland, 33607 Pessac, France
E-mail: kuhn@enscbp.fr
A. Karajić
Novel Device Lab
University of Cincinnati
Cincinnati, OH 45221, USA
P. N. Bartlett
School of Chemistry
University of Southampton
Southampton SO17 1BJ, UK
N. Mano
Centre de Recherche Paul Pascal (CRPP)
CNRS UMR 5031
Univ. Bordeaux
115 Avenue du Docteur Schweitzer, 33600 Pessac, France

ⓘ The ORCID identification number(s) for the author(s) of this article can be found under https://doi.org/10.1002/adfm.202210638.

1. Introduction

Electroanalytical methods are used in a broad range of scientific disciplines from fundamental research to different applications, such as biological or environmental sensors as well as in fuel and solar cells.[1] Consequently, there is a strong interest in optimizing their sensitivity and selectivity.[2] One way to address these issues is to use redox cycling (RC) as a powerful strategy to amplify faradaic currents in electroanalytical measurements, which can enhance the sensitivity through fast multiple oxidation and reduction events.[3] In order to implement RC, two closely spaced and individually addressable electrodes are biased simultaneously to potentials above and below the formal redox potential of the analyte. This method has been applied in scanning electrochemical microscopy (SECM) for the detection of individual molecules that were confined within the space between a tip and a conducting surface.[4,5] The current amplification which can be achieved through redox cycling strongly depends on the time that a redox active molecule needs to diffuse back and forth between the oppositely polarized electrodes, and therefore the distance between the cathode and anode is a critical parameter that needs to be carefully tuned and optimized, as well as their respective surface areas.[6]

Thin-layer electrochemical cells comprising two planar electrodes separated by a thin layer of liquid are the most frequently used type of redox cycling devices.[7] In order to reduce the gap size it is necessary to use cleanroom facilities and multi-step photo- or e-beam lithography techniques as demonstrated in the pioneering work of Lemay et al., where the sensitivity of these devices allows even single-molecule detection.[8–11] While these devices have many advantages, there is still a need for simplified elaboration processes to open up their use to a broader range of applications.[12] Many reported RC devices are based on such a planar electrode geometry either in a 2D or 3D configuration,[13,14] because the design of thin layer electrochemical cells with electrodes having more complex geometries (e.g., curved electrode surfaces with a cylindrical geometry) would be a real challenge for standard microfabrication techniques. In addition to challenging fabrication, the so far reported devices often need external pumping of the analyte into the reaction space, for example based on microfluidic systems.
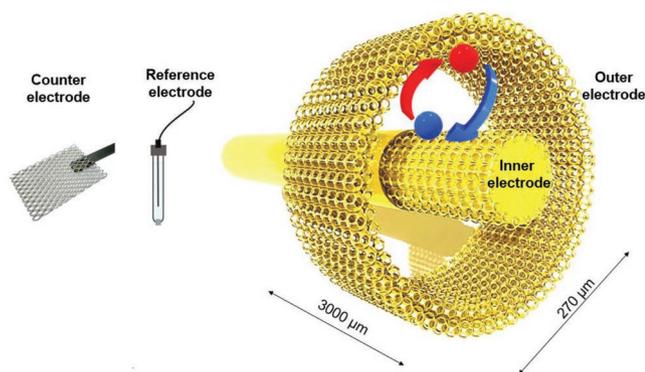
Figure 1. Schematic representation of a cylindrical coaxial twin electrode set-up for redox cycling. A fast exchange of the oxidized (●) and reduced (●) form of the analyte is occurring between the inner and outer electrode. Measurements are performed with respect to external reference and counter electrodes.

2. Results and Discussion

The strong demand for high-performance electrochemical devices leads to the need to improve their electrochemical features through an appropriate choice of electrode material, surface properties, as well as the architectures of the device. One way of improving the efficiency of different setups is by using porous electrodes. Porous materials can be easily synthesized by perfusing a target material through a temporary template. Templates such as nanoparticles are used to generate highly organized functional materials with well-defined morphologies.

2.1. Electrode Elaboration

The Langmuir–Blodgett (LB) technique enables the assembly of micrometer-sized silica particles into a stack of successive monolayers on the gold wire substrates. One of the biggest advantages of the LB process over other existing techniques is the precise control of the template architecture at the single-layer level.[16] After spreading the silica particles at the water-air interface of the LB trough, the compression of the film is controlled by measuring the surface pressure as a function of the film area. Once a compact Langmuir film is formed, the silica monolayers are transferred onto the surface of the oxygen-plasma-treated gold microwires, and in that way, a colloidal crystal is obtained (**Figure 2**a).

Such a colloidal crystal is used as a template for the potentiostatic infiltration of alternating gold–nickel–gold layers (Figure 2b).[17] In the resulting metal/silica composite, nickel acts as a sacrificial separator between two gold layers, which later can be removed during a wet etching step in diluted nitric acid (Figure 2c). After the nickel layer has been removed, structural integrity is preserved through infiltration of diluted varnish at the two extremities of the structure. The scanning electron microscopy (SEM) image of a cross-section at the extremity of the electrode reveals the presence of a varnish layer between the two gold electrodes, maintaining the distance inbetween (Figure S1, Supporting Information). In order to electrically address the outer gold electrode, a silver microwire is attached directly to the surface and connected with silver paste. Then, the colloidal silica template is dissolved in diluted hydrofluoric acid and the final microporous electrode structure is obtained (Figure 2d).

In this work, we report an original miniaturized three-dimensional electrode architecture for RC (**Figure 1**).

Following an adapted bottom-up approach, porous cylindrical electrodes can be generated in a coaxial configuration, having a high active surface area which results in a very compact device design.[15] The originality of the device relies on the concentric cylindrical architecture, and, even more importantly, a well-defined and perfectly controllable porosity. This allows delivering constantly fresh analyte by natural diffusion through the pores of the outer electrode into the gap where redox cycling occurs. Consequently, no external feeding of the device with an analyte is necessary, and the cylindrical shape guarantees 100% collection efficiency. In comparison to the reported techniques, the straightforward and low-cost bottom-up synthesis allows fine-tuning the thickness of the electrodes, the pore size, and the distance between the electrodes. The synergy between the ordered porosity and confined geometry results in significant amplification without the need for complex technology or facilities. Mechanical stabilization of the coaxial architecture allows the prevention of short circuits and ensures the stability of the device over long time periods. All the above-mentioned parameters can be adjusted in order to optimize the redox cycling efficiency.
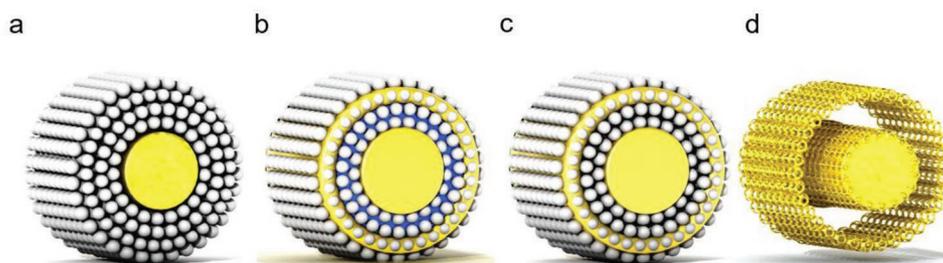

Figure 2. Scheme illustrating the elaboration steps of a miniaturized coaxial macroporous twin electrode. a) Gold microwire (250 μm) covered with a predefined number of 1 μm silica particle layers. b) Electrodeposition of the gold–nickel–gold layer through the colloidal silica template. c) Structure obtained after the selective dissolution of the nickel layer. d) Final electrode structure obtained after the dissolution of the silica template.
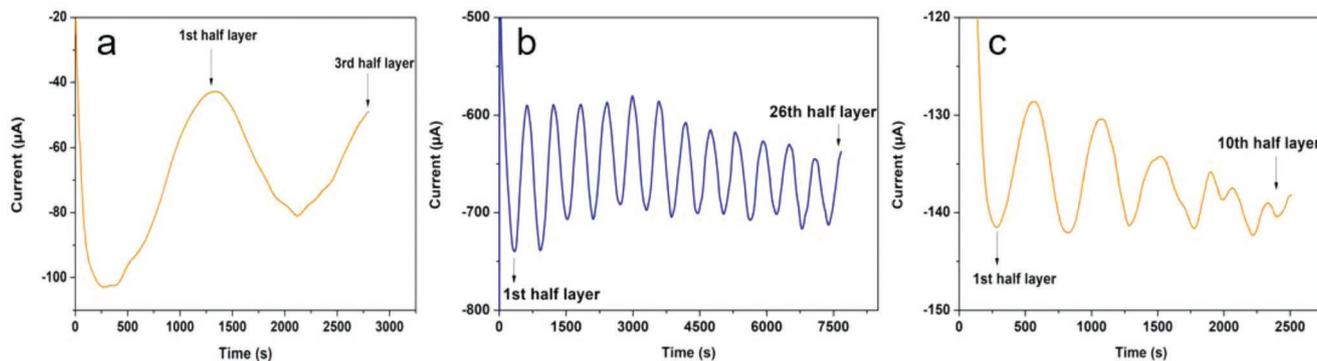
**ADVANCED
SCIENCE NEWS**
www.advancedsciencenews.com

**ADVANCED
FUNCTIONAL
MATERIALS**
www.afm-journal.de

Figure 3. Examples of chronoamperometric curves recorded during the electrodeposition of a) the inner gold, b) the intermediate nickel, and c) the outer gold layers throughout the colloidal silica template.

Highly precise control over the thickness of the metal growing through the silica template is achieved by tracking the current oscillations vs. time (**Figure 3**). These periodic variations of current are due to a change in the electroactive surface area while the metal is infiltrating the template. This allows a fine-tuning of the thickness and, most importantly, of the distance between the two final macroporous gold electrodes. As shown in Figure 3a, the inner electrode consists of 1.5 layers of porous gold, whereas the outer electrode is composed of 5.5 porous gold layers (Figure 3c). The distance between the two final gold electrodes is defined by 13.5 layers of nickel (Figure 3b), which corresponds to ≈15 μm. If necessary, the size of this gap can be tuned from the submicrometer level to several tens of microns. Electrodeposition is usually terminated at the half-layer level to ensure completely open pores.

2.2. Electrode Characterization

2.2.1. SEM Characterization

SEM characterization was carried out after every fabrication step as presented in **Figure 4**. It shows the alternating gold–nickel–gold layers having a thickness that is in agreement with the one predicted by the current oscillations. Figure 4b has been recorded after nickel dissolution, with preserved silica beads sandwiched between the two gold electrodes. Finally, Figure 4c illustrates the final electrode structure after the removal of the silica beads, indicating a regular macroporous structure, as well as a uniform thickness and homogenously distributed pores.[18]

2.2.2. Electrochemical Response

The electrochemical functionality of the coaxial twin electrode system was tested by cyclic voltammetry (CV) to confirm that the two electrodes were independently addressable.

The outer and the inner electrodes were separately connected to the potentiostat and their CVs were recorded in pure 0.5 M H_2SO_4 as supporting electrolyte (**Figure 5**a). The gold-oxide stripping peak around 0.9 V is used to calculate the electrochemical active surface area by dividing the corresponding charge by 390 μC cm^{-2}.[19]

To make the two electrodes easily distinguishable in terms of their electrochemical characteristics, the outer porous layer
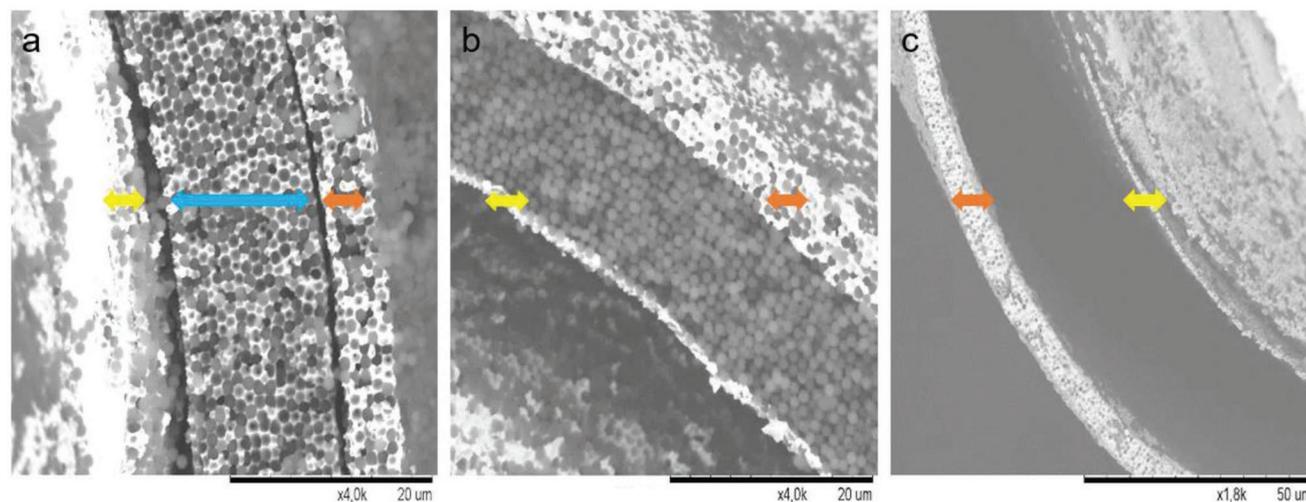

Figure 4. SEM characterization of a coaxial twin electrode architecture composed of alternating gold (yellow arrow)–nickel (blue arrow)–gold (orange arrow) layers a) in the presence of the silica template, b) after the dissolution of nickel, and c) of the final architecture after the dissolution of the silica particles.
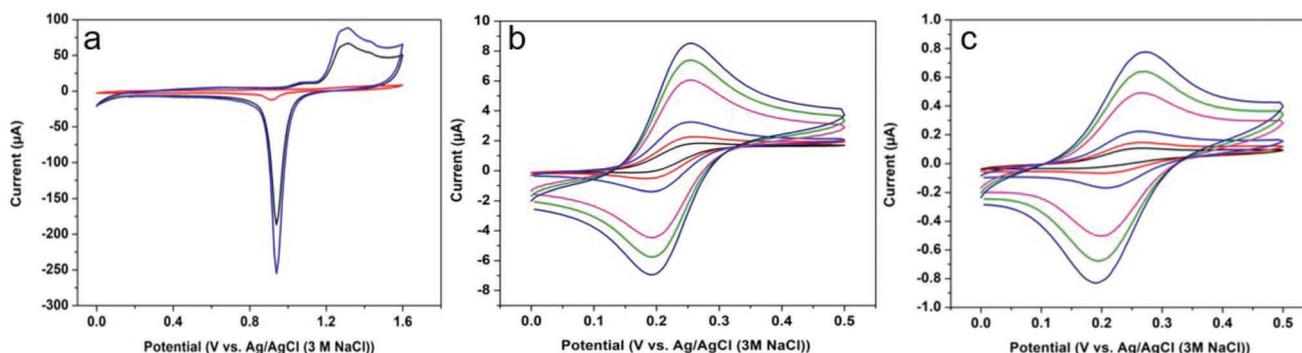
ADVANCED
SCIENCE NEWS
www.advancedsciencenews.com

ADVANCED
FUNCTIONAL
MATERIALS
www.afm-journal.de

Figure 5. a) Electrochemical characterization of the structural stability and electrical independency of the coaxial electrodes for the inner (red), outer (dark blue) and short-circuited (light blue) electrodes recorded in 0.5 M sulfuric acid at 100 mV s^{-1}; b,c) Cyclic voltammograms of the outer and inner electrodes in 1 mM ferrocene methanol in 0.1 M KNO$_3$ recorded at 5, 10, 25, 100, 150 and 200 mV s^{-1}, respectively.

has been chosen to be much thicker in comparison to the inner one, with active surface areas of 0.4 cm^2 and 0.04 cm^2, respectively (Figure 5a, red and black curves). In the next step, both electrodes were on purpose short-circuited and the total calculated surface area of 0.44 cm^2 corresponds to the sum of the surface areas of the two individual electrodes (Figure 5a, blue curve). This confirms the structural integrity of the architecture and the absence of a short circuit between the outer and the inner electrode, despite their micrometric separation.

A first evaluation of the functionality of the elaborated architecture was carried out by recording CVs in 1 mM ferrocene methanol solution prepared in 0.1 M KNO$_3$ as a function of the scan rate for the outer electrode (Figure 5b) while the inner electrode was kept at a floating potential (single mode measurement) and vice versa (Figure 5c). The shape of the recorded CVs is characteristic of a diffusion-controlled process of redox species present in solution with the faradaic current being directly proportional to the square root of the scan rate (Figure S2, Supporting Information) in agreement with the Randles–Ševčik equation.[20]

In the next set of experiments, chronoamperometry has been used as the first technique to illustrate the efficiency of redox cycling with ferrocene methanol as an analyte. Two sets of experiments were performed to characterize the twin electrode system concerning redox cycling. In the first experiment (**Figure 6a**), the outer electrode was used as a generator while the inner electrode served as a collector. The generator electrode was kept at 0.3 V to oxidize ferrocene methanol and subsequently reduce it at the collector electrode, which is kept at a potential of 0.0 V. The recorded currents show a significant signal amplification when comparing the currents obtained in the single electrode mode (Figure 6b, black curve) and redox cycling mode (Figure 6b, red and blue curves).

The amplification factor (*f*) can be calculated in a first-order approximation by dividing the stationary current of the generator electrode at long times (80 s) in the redox-cycling mode ($I_{r.c.}$) by the current obtained when the same electrode is used in a single electrode mode (without recycling effect ($I_{n.r.c.}$).[6]

$$f = I_{r.c.}/I_{n.r.c.} \tag{1}$$

The calculated amplification factor for the present configuration is 10. Since the redox cycling effect is strongly influenced by the geometry of the electrode arrangement, affecting the diffusional transport, it has been suggested by Kätelhön and Wolfrum that the key number that reflects these design features should be the collection efficiency (η).[1] The collection efficiency η is defined by the ratio of the currents at the generator (I_{gen}) and collector I_{col} electrodes.[21]

$$\eta = I_{gen}/I_{col} \tag{2}$$

In the present case, the collection efficiency was found to be 90%.

In the second set of experiments (Figure 6c), the reversed configuration was used, with the inner electrode acting as the generator and the outer as the collector electrode. By dividing the stationary currents of the obtained amperograms (Figure 6d), the calculated amplification factor was 115, while the collection efficiency reached 100%.

Thus, when the inner electrode is the generator, the amplification as well as the collection efficiency is considerably improved, which can be explained by two types of phenomena. First, the outer electrode has a ten times higher surface area than the inner one (vide supra) and therefore can collect easily all oxidized species produced by the inner electrode and convert them back by reduction. Second, there is a fundamental difference between the two configurations. When the inner electrode is the generator, all species produced by oxidation are converted back into the reduced form by the outer one without the possibility to escape into bulk, causing a drastic increase in the amplification factor (Figure 6c). On the contrary, when the oxidized form is generated by the outer electrode, a certain fraction is diffusing into the confined space toward the inner electrode and will be recycled, but an important part can also diffuse into the bulk solution and consequently is lost for the recycling process (Figure 6a).

Theoretical diffusion limited recycling currents for a single molecule in a nanogap can be calculated according to Equation (3), with the assumption that the gap is much longer than wide.[4,22]
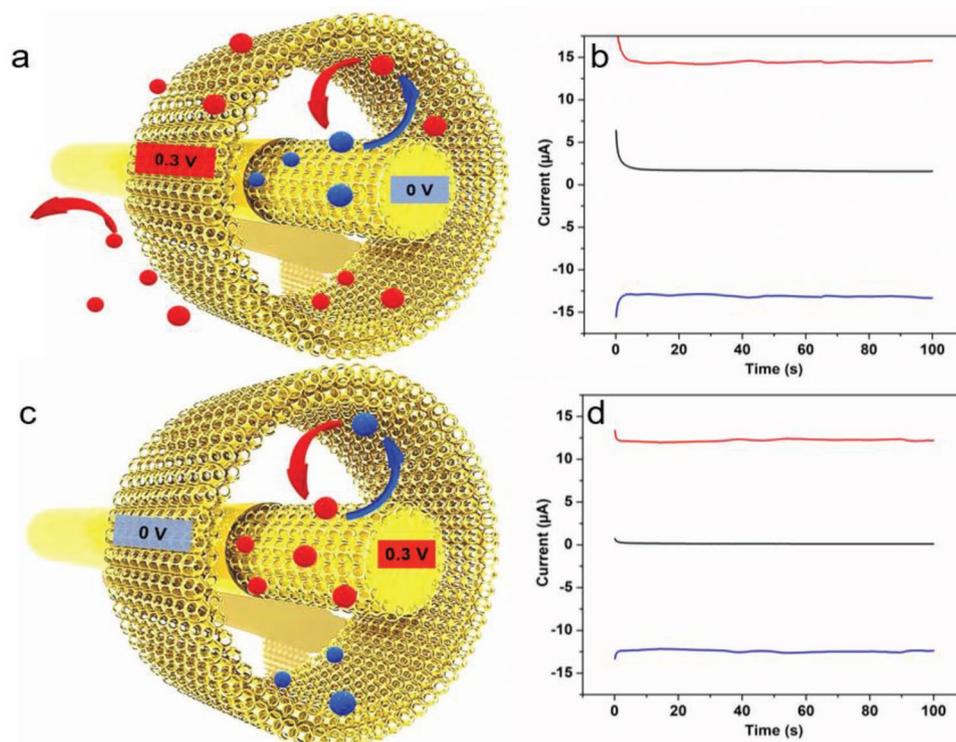
$$i_R = eD/z^2 \tag{3}$$

Figure 6. a) Schematic representation of the redox cycling process and distribution of the oxidized (●) and reduced (●) ferrocene methanol species when the outer electrode (generator) is polarized to 0.3 V, while the inner one (collector) is kept at a constant potential of 0 V. b) Amperometric response showing the comparison of the single electrode mode when the outer electrode is polarized at 0.3 V, while the potential of the inner one is floating (black curve), and the redox cycling mode, where the inner electrode is biased at a constant potential of 0 V (red and blue curves for the outer and inner electrode respectively). c) Schematic representation of the redox cycling process when the inner electrode is the generator, while the outer one is the collector. d) Amperometric response showing the comparison of the single electrode mode, when the inner electrode is polarized at a potential of 0.3 V, while the outer one is at a floating potential (black curve), and the redox cycling mode with the inner electrode acting as a generator polarized at 0.3 V, and the outer one being the collector at a constant potential of 0 V (red and blue curves for the inner and outer electrode respectively).

with a diffusion coefficient (D) of 7.5×10^{-6} cm^2 s^{-1},[23] e being the charge of an electron and z the gap width. A single ferrocene methanol molecule in a 15 µm gap would be expected to produce a current of 5.34×10^{-19} A. When applying this calculation to a finite number of molecules, the concentration and the volume of the gap have to be known. The latter can be calculated by subtracting the volume of the outer from the inner electrode cylinder, since all dimensional parameters are known, due to precise control of the manufacturing process. In the estimated 0.0245 mm^3 gap, 1.47×10^{13} molecules will be present for a 1 mM ferrocene methanol solution, consequently generating a current of 8×10^{-6} A.

These theoretical calculations are based on the assumption that the surface is flat or in other words that the roughness is neglectable. In the case of the porous systems, porosity is increasing the surface area available for the reaction in comparison to the flat analog. Therefore, the roughness of the electrodes needs to be considered when calculating the theoretical current. The theoretical roughness factor (R_{th}) is:[24]

$$R_{th} = \sqrt{\frac{4}{3}\pi n} \qquad (4)$$

with n being the number of pore layers.

However, as in the present work a fast redox couple is used, molecules are only reacting at the outermost pore layer and thus n is 0.5, which corresponds to a roughness factor of 1.8. The value of the corrected current is therefore 14×10^{-6} A and is in very good agreement with the steady-state currents experimentally obtained from the chronoamperograms 14×10^{-6} A (Figure 6b) and 12×10^{-6} A (Figure 6d).

In a complementary series of experiments, cyclic voltammograms were recorded for the configuration showing the most efficient redox cycling effect (**Figure 7**a–c). Voltammograms were compared for the single electrode mode and the redox cycling mode of the inner electrode. Once the electrodes are polarized to sufficiently high anodic/cathodic potentials, the ferrocene methanol molecules participate in a series of repeated redox reactions, leading to redox cycling, with an efficiency that depends on the characteristic time window of the experiment (i.e., the chosen scan rate).

For 5 mV s^{-1} as the slowest scan rate, the current amplification is very pronounced (Figure 7a). Calculating at the peak potential the ratio of the oxidation current in the redox cycling and in the single electrode mode, the amplification factor (f) is 84, which is very similar to the one obtained from the chronoamperometric measurements. At a shorter time scale (i.e., 100 mV s^{-1}), the amplification factor decreases to 28 (Figure 7b),
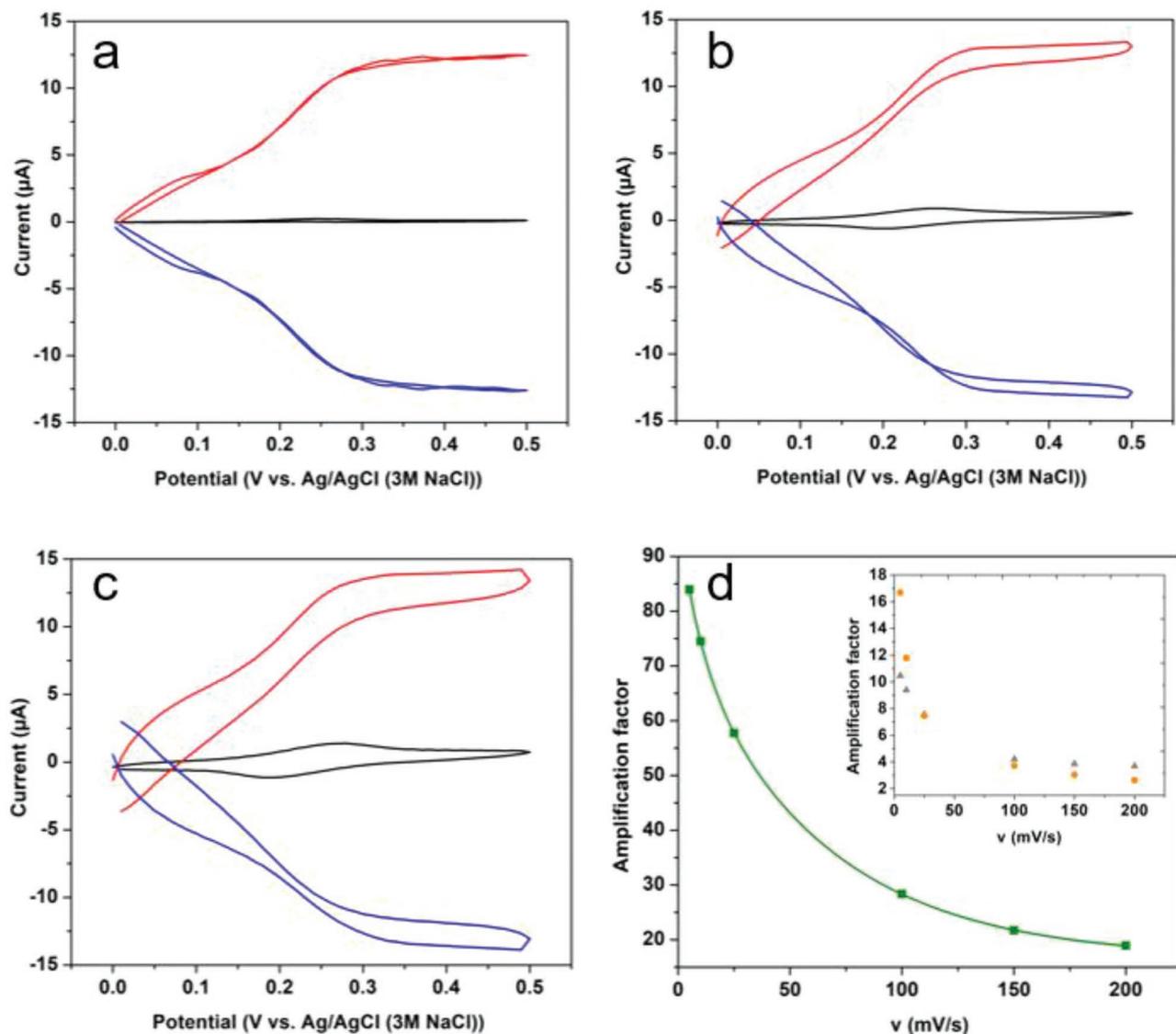
Figure 7. Illustration of the signal amplification measured by cyclic voltammetry at different scan rates: a) 5 mV s^{-1}, b) 100 mV s^{-1}, and c) 200 mV s^{-1}. Comparison between the single electrode mode where the potential of the inner electrode is swept between 0.0 and 0.5 V while the outer is at a floating potential (black curve), and the redox cycling mode where the inner electrode acts as the generator and the outer as the collector (red and blue curves respectively). d) Correlation between scan rate and amplification factor obtained from the experimental data (■) with an inset showing the theoretical amplification factor calculated according to the Randles–Ševčik equation (●) and the corrected experimental amplification factor (▲).

and for the highest scan rate (200 mV s^{-1}) it drops down to 18 (Figure 7c). At even higher scan rates, the amplification effect disappears, as the redox species do not have enough time to travel back and forth between the two electrodes (Figure 7d, black curve). At high scan rates, steady-state redox cycling is not fully established between the two electrodes.[25] The impact of the scan rate on the thickness of the diffusion layer causes higher amplification factors in amperometric measurements compared to cyclic voltammetry.

The limiting recycling current for the two planar electrodes separated by a thin layer of fluid can be estimated by Equation (5):[26]

$$i_R = (nFADc)/z \tag{5}$$

Since the amplification factor is defined as the ratio between the recycling current and the current without recycling effect, obtained from the Randles–Ševčik equation, f can be expressed as:

$$f = \frac{i_R}{i_p} = \left(\frac{DRT}{nFv}\right)^{1/2} \frac{1}{0.4463z} \tag{6}$$

with a diffusion coefficient D of 7.5×10^{-6} cm^2 s^{-1},[23] R the gas constant, T the temperature, n the number of electrons transferred per redox event, F the Faraday constant, v the scan rate, and z the gap size.

The influence of the roughness of the electrodes was included in the calculation and the results are shown in the inset of Figure 7d. For example, for a distance of 15 μm and

for the slowest scan rate, an amplification factor of 16 is calculated while a factor of 2 is obtained for the highest scan rate. In order to illustrate the variation of the amplification as a function of the distance between the inner and outer electrode, we increased the gap from 15 µm to 25 µm. Even though this new distance is relatively big, redox cycling still occurs (Figure S3, Supporting Information). Plateau currents, which were at the level of 12 µA for 15 µm, decrease by a factor 10, which is in good agreement with what is theoretically expected. Consequently, for electrodes with the 25 µm gap, the amplification factor will be smaller, which is in agreement with previous work as with Equation (6).

One interesting observation is that the values in Figure 7d (green curve) are smaller than the experimentally determined amplification factors of 83 and 18 respectively. This discrepancy might be due to the fact that the currents measured for the inner electrode in the single electrode mode (black curves in Figure 7a–c) are underestimated, as the diffusion of the redox probe toward the inner electrode is restricted by the presence of the outer electrode. Therefore the reacting redox probe originates essentially from the thin layer between the outer and inner electrode, comparable to the situation encountered in thin film electrochemistry.[27,28]

To confirm this hypothesis we performed a control experiment with an individual macroporous gold wire with dimensions and a roughness identical to those of the inner electrode used in the coaxial setup (Figure S4, Supporting Information). In this case, the oxidation and reduction currents of ferrocene methanol are approximately ten times higher than those measured for the inner electrode in the coaxial setup. Based on this observation, it is possible to recalculate corrected amplification factors and the results are illustrated by the inset in Figure 7d (grey triangles). As can be seen, this leads to a good agreement between the experimental and theoretical values, except for slow scan rates. The observed discrepancy between theoretically expected and experimentally measured amplification values at low scan rates can be rationalized and understood by considering what happens with the size of the diffusion layer in the vicinity of these electrodes as a function of scan rate. At low scan rates, the diffusion layer has the time to expand and its characteristic thickness becomes bigger than the morphological features (pores) of the electrode. Thus, the measured currents are comparable to those that would be obtained for a flat analog. Consequently, the correction factor that we introduced, for taking into account the contribution of the porous first half layer in terms of active surface area, is not really justified and results in a slight overestimation of the theoretical current (and the amplification factor) based on the Randles–Ševčik equation. On the other hand, for higher scan rates, the diffusion layer is relatively thin and thus follows the contour of the porous half layer, thus justifying the use of the correction factor related to surface enhancement by porosity.

Even though the proposed devices have a 300 times bigger distance between electrodes, the obtained amplification factors are comparable or even higher in comparison to what has been reported in previous studies,[29,30] due to a synergy between the geometry and porous high surface area electrodes.

3. Conclusion

In this contribution, we describe a coaxial macroporous redox cycling device, elaborated by following a straightforward, low-cost and scalable bottom-up strategy, as there is no need for cleanroom facilities nor expensive microfabrication techniques.[31] In contrast to the state-of-the-art, the device is based on two cylindrical macroporous gold electrodes with a tunable gap. A significant redox cycling effect has been observed, which is in good agreement with what is predicted by theory. The device is versatile, as several parameters such as the gap, the thickness of the individual electrodes and the pore size can be adjusted to optimize the performance as a function of the nature of the probe molecule. Gold was selected for this study because of its inertness toward the chemicals that are used in the process of etching the nickel layer as well as the silica beads. Furthermore, the ease of post-modification of the gold surface also opens an interesting perspectives for the development of miniaturized fully integrated electrochemical (bio)sensing and point-of-care devices.

4. Experimental Section

Electrodeposition of Alternating Metal Layers into a Colloidal Template: Electrodeposition of alternating gold–nickel–gold (Au–Ni–Au) metal layers was performed successively using commercially available electroplating solutions, ECF60 (Metalor) and semi-bright nickel solution (AlfaAesar). Electrodeposition was performed with a potentiostat (PalmSens4) at a constant potential in a three-electrode set-up consisting of the colloidal crystal template modified gold microwire (250 µm diameter, AlfaAesar) as a working electrode. Ag/AgCl (3 M NaCl) and a cylindrical Kapton-carbon foil were used as reference and counter electrode, respectively. The electrode potentials applied for the electrodeposition of alternating metal layers were −0.53 V, −0.85 V, and −0.70 V for the inner gold layer, the nickel layer, and the outer gold layer, respectively. If not stated otherwise, all electrode potentials were defined versus the Ag/AgCl (3 M NaCl) reference electrode.

Etching of the Nickel Layer: The nickel layer was etched with 30% nitric acid for one day at ambient temperature. Samples were washed with MQ water to remove dissolved nickel and nitric acid. The set-up was equipped with a stirrer to facilitate the etching process.

Stabilization of the Final Coaxial Structure: To stabilize the final coaxial structure, the bottom part was infiltrated with varnish diluted with acetone (1:5 v/v) by dip coating and subsequent drying. The outer electrode was electrically connected with a silver microwire (50 µm), which was attached to the surface of the electrode with a drop of silver paint (Agar silver paint, Agar). Just next to the connection, the diluted varnish was drop casted onto the structure. The electrode was dried over night at ambient temperature and silica particles were etched in 5% HF prior to electrochemical testing. The elaboration process was followed by SEM experiments, carried out on a Hitachi TM-1000 tabletop microscope.

Electrochemical Characterization of the Structure: The final coaxial macroporous system with two independently addressable electrodes was tested by cyclic voltammetry (CV) using a CHI bipotentiostat (Austin, TX, USA). CVs were recorded using a three-electrode set-up composed of the working electrode (coaxial sample), a reference electrode (Ag/AgCl) and a counter electrode (platinum wire) in a potential window from 0.0 V to 1.6 V, with 0.5 M sulfuric acid (Sigma-Aldrich) as supporting electrolyte and at a scan rate of 100 mV s⁻¹. The coaxial electrodes were connected either separately or together, cycled several times until the current reached a constant value. For additional electrochemical measurements 1 mM ferrocene methanol (Sigma-Aldrich) in 0.1 M KNO₃ (Sigma-Aldrich) was used.

**ADVANCED
SCIENCE NEWS**

www.advancedsciencenews.com

**ADVANCED
FUNCTIONAL
MATERIALS**

www.afm-journal.de

Supporting Information

Acknowledgements

Conflict of Interest

The authors declare no conflict of interest.

Data Availability Statement

The data that support the findings of this study are available from the corresponding author upon reasonable request.

Keywords

[1] E. Kätelhön, B. Wolfrum, *Rev. Anal. Chem.* **2012**, *31*, 7.
[2] H. R. Zafarani, K. Mathwig, S. G. Lemay, E. J. R. Sudhölter, L. Rassaei, *ACS Sens.* **2016**, *1*, 1439.
[3] D. Han, L. P. Zaino, K. Fu, P. W. Bohn, *J. Phys. Chem. C* **2016**, *120*, 20634.
[4] F. R. F. Fan, A. J. Bard, *Science (1979)* **1995**, *267*, 871.
[5] A. J. Bard, M. v. Mirkin, P. R. Unwin, D. O. Wipf, *J. Phys. Chem.* **1992**, *96*, 1861.
[6] B. Wolfrum, E. Kätelhön, A. Yakushenko, K. J. Krause, N. Adly, M. Hüske, P. Rinklin, *Acc. Chem. Res.* **2016**, *49*, 2031.
[7] M. A. G. Zevenbergen, B. L. Wolfrum, E. D. Goluch, P. S. Singh, S. G. Lemay, *J. Am. Chem. Soc.* **2009**, *131*, 11471.
[8] S. G. Lemay, S. Kang, K. Mathwig, P. S. Singh, *Acc. Chem. Res.* **2013**, *46*, 369.
[9] M. A. G. Zevenbergen, P. S. Singh, E. D. Goluch, B. L. Wolfrum, S. G. Lemay, *Nano Lett.* **2011**, *11*, 2881.
[10] S. Kang, A. F. Nieuwenhuis, K. Mathwig, D. Mampallil, Z. A. Kostiuchenko, S. G. Lemay, *Faraday Discuss.* **2016**, *193*, 41.
[11] M. A. G. Zevenbergen, D. Krapf, M. R. Zuiddam, S. G. Lemay, *Nano Lett.* **2007**, *7*, 384.
[12] H. R. Zafarani, K. Mathwig, E. J. R. Sudhölter, L. Rassaei, *J. Electroanal. Chem.* **2016**, *760*, 42.
[13] E. O. Barnes, G. E. M. Lewis, S. E. C. Dale, F. Marken, R. G. Compton, *Analyst* **2012**, *137*, 1068.
[14] K. Ino, Y. Kanno, T. Nishijo, H. Komaki, Y. Yamada, S. Yoshida, Y. Takahashi, H. Shiku, T. Matsue, *Anal. Chem.* **2014**, *86*, 4016.
[15] A. Karajic, S. Reculusa, M. Heim, P. Garrigue, S. Ravaine, N. Mano, A. Kuhn, *Adv. Mater. Interfaces* **2015**, *2*, 1500192.
[16] S. Reculusa, M. Heim, F. Gao, N. Mano, S. Ravaine, A. Kuhn, *Adv. Funct. Mater.* **2011**, *21*, 691.
[17] P. N. Bartlett, P. R. Birkin, M. A. Ghanem, *Chem. Commun.* **2000**, *17*, 1671.
[18] P. N. Bartlett, J. J. Baumberg, P. R. Birkin, M. A. Ghanem, M. C. Netti, *Chem. Mater.* **2002**, *14*, 2199.
[19] S. Trassatti, O. A. Petrii, *Pure Appl. Chem.* **1991**, *63*, 711.
[20] D. Jain, A. Karajic, M. Murawska, B. Goudeau, S. Bichon, S. Gounel, N. Mano, A. Kuhn, P. Barthélémy, *ACS Appl. Mater. Interfaces* **2017**, *9*, 1093.
[21] A. J. Bard, J. A. Crayston, G. P. Kittlesen, T. V. Shea, M. S. Wrighton, *Anal. Chem.* **1986**, *58*, 2321.
[22] H. S. White, K. McKelvey, *Curr. Opin. Electrochem.* **2018**, *7*, 48.
[23] V. Mishyn, P. Aspermair, Y. Leroux, H. Happy, W. Knoll, R. Boukherroub, S. Szunerits, *Surfaces* **2019**, *2*, 193.
[24] A. Kuhn, M. Heim, in *Springer Handbook of Electrochemical Energy* (Eds: C. Breitkopf, K. Swider-Lyons), Springer Berlin Heidelberg, Berlin, Heidelberg **2017**, p. 143.
[25] Á. Molina, J. González, F. Martínez-Ortiz, R. G. Compton, *J. Phys. Chem. C* **2010**, *114*, 4093.
[26] L. B. Anderson, C. N. Reilley, *J. Electroanal. Chem.* **1965**, *10*, 295.
[27] K. Aoki, K. Tokuda, H. Matsuda, *J. Electroanal. Chem.* **1983**, *146*, 417.
[28] K. Aoki, K. Tokuda, H. Matsuda, *J. Electroanal. Chem.* **1984**, *160*, 33.
[29] S. Sarkar, K. Mathwig, S. Kang, A. F. Nieuwenhuis, S. Lemay, *Analyst* **2014**, *139*, 6052.
[30] B. Wolfrum, M. Zevenbergen, S. Lemay, *Anal. Chem.* **2008**, *80*, 972.
[31] M. Hüske, R. Stockmann, A. Offenhäusser, B. Wolfrum, *Nanoscale* **2014**, *6*, 589.